Physical Modeling and Parameter Extraction for Event-based Vision Sensors

Andreas Suess, Menghan Guo, Rui Jiang, Xiaozheng Mou, Qiping Huang, Wenlei Yang, Shoushun Chen

OMNIVISION, 4275 Burton Drive, Santa Clara, CA 95054 USA

***Abstract*—Latency and noise are crucial aspects of Event-based Vision Sensors. Yet, in simulators used to create synthetic event data these effects are predominantly modeled phenomenologically and are rarely calibrated to actual measurements or circuit simulations. This work presents a physics-based latency and noise model achieving strong resemblance with circuit simulations and measurements. The model is computationally efficient enough to be suitable for camera simulation. This enables accurate training data synthesis for algorithm development and guides sensor design.**

I. Introduction

Event-based Vision Sensors (EVS) experience an increasing commercial interest [1]–[6]. Simulators are commonly employed to synthesize events from videos connecting sensor design and algorithm development depending on application requirements [7]–[10]. Today's simulators, however, are mostly phenomenological and lack calibration against actual sensor designs using simulation or measurements [7]–[9]. [7], [8] introduced adaptive frame-upsampling before event generation and randomized the contrast threshold to allow for generalization of trained algorithms to sensor variability. [9] introduced modeling of pixel non-idealities. Pixel latency was modeled by a single pole IIR filter whose bandwidth scales proportional to the light level. A pixel-wise Gaussian-distributed contrast threshold models sensor non-uniformity. Periodic leak events and Poisson sampled noise events were introduced into the event stream, whereas the noise events were scaled with luma level to capture light dependence. [10] extended the attempt towards realistic event simulation by calibrating a more complex semi-empirical pixel latency model to circuit simulations. Furthermore, refractory period and latency from the peripheral circuitry were modeled. [10] presented reasonable matching of pixel latency at higher photocurrents, but matching at low light was limited. Conversely to [9], [10] did not inject noise events into a pre-computed noise-free event stream, but directly added random noise to the signal amplitude before the comparators. However, bandwidth was not considered. Modeling the noise directly in the voltage domain is crucial to match effects such as time-stamp uncertainty caused by noise, or fire probabilities in case the signal is in proximity of the contrast threshold. Leak events should also be modeled in the voltage domain to reflect the signal dependence of leak events.

In order to advance event simulators, this work derives physical models for latency and noise considering bias and temperature conditions (Sec. II and Sec. III). It will be shown that the models surpass the matching to circuit simulations achieved in [10] (Sec. II). Views on parameter extraction will be outlined and the model is validated against measurements (Sec. V).

II. Large-signal pixel latency model

Fig. 1 depicts a simplified schematic of the analog portion of an event-based vision pixel. The photodiode current, $I_{\text{PD}} = I_{\text{photo}} + I_{\text{dark}}$, is converted into a logarithmic voltage measured at node V_{FE}. M_{SF} decouples the front-end circuit from a difference-detecting switched-capacitor filter of gain G. Subsequent comparators determine if a temporal contrast beyond a predefined

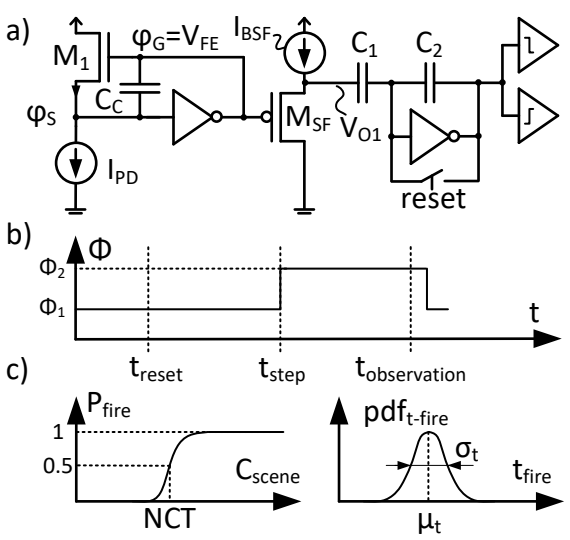

Figure 1. a) analog EVS pixel circuit schematic, b) temporal contrast measurement timing diagram, and c) fire probability "S-curve" and time-stamp distributions.

threshold is detected. Fig. 1b illustrates the temporal contrast step measurement technique [11], [12]. Fig. 1c depicts that at increasing contrast step, $C = [\Phi_2 - \Phi_1]/\Phi_1$, a corresponding increase in event firing probability is observed. The contrast at which the probability amounts to $50\,\%$ is termed the Nominal Contrast Threshold (NCT) [3]. This measure is of relevance as it indicates the effective contrast threshold of a given pixel at a given measurement condition. Ideally, the transition from low firing probability to high firing probability is sharp around that NCT value. However, temporal noise causes randomness in trigger probability and results in the shape that coins this characteristic "S-curve." Clearly, the slope of the S-curve is important to characterize a pixel. The right part of Fig. 1c illustrates the event firing time probability distribution. The firing time has an offset latency μ_t determined by transients to charge/discharge nodes in the analog portion of the event pixel, as well as propagation and scan delays from the digital peripheral readout. Event pixels exhibit a timing uncertainty σ_t which is characterized by electronic noise and randomness in the peripheral readout. For S-curve characterization, it is preferred to select a small region of interest to separate the readout delay and uncertainty from pixel latency. It is clear that merits like NCT or firing time strongly depend on: radiance, the time interval of pixel reset and applied scene contrast step, as well as the overall observation time under which e.g. noise is permitted to elevate above a contrast threshold. This implies that such merits do not have full predictive value at operation under varying conditions. Therefore, a model-based approach is required.

All transistors are assumed to operate in weak inversion and

saturation and are modeled as:

$$I_{\mathrm{D}} = I_0 \cdot \frac{W}{L} \cdot \exp\left(\frac{\varphi_{\mathrm{G}} - \zeta \cdot \varphi_{\mathrm{S}}}{\zeta \cdot V_{\mathrm{T}}}\right) \quad \text{(NMOS)}$$
$$I_{\mathrm{D}} = I_0 \cdot \frac{W}{L} \cdot \exp\left(\frac{-\varphi_{\mathrm{G}} + \zeta \cdot \varphi_{\mathrm{S}}}{\zeta \cdot V_{\mathrm{T}}}\right) \quad \text{(PMOS)}, \qquad (1)$$

with drain current I_{D}, specific current I_0, width W and length L, gate and source potentials φ_{G} and φ_{S}, slope-factor $\zeta \approx 1..1.4$ and thermal voltage $V_{\mathrm{T}} = k_{\mathrm{B}} \cdot \theta / q$ at temperature θ, with Boltzmann constant k_{B} and elementary charge q. The inverting amplifier in the feedback path of the logarithmic amplifier is modeled by an affine-linear relation: $\varphi_{\mathrm{G1}} = A \cdot [V_{\mathrm{x}} - \varphi_{\mathrm{S1}}]$, with amplifier gain A and some offset term V_{x}. With $I_{\mathrm{D1}} = I_{\mathrm{PD}}$ the stationary solution is given by:

$$t \to \infty \Rightarrow \varphi_{\mathrm{G1}} = \frac{A \cdot \zeta \cdot V_{\mathrm{x}}}{\zeta + A} \cdot \left[1 + \ln\left(\frac{I_{\mathrm{PD}}}{I_0 \cdot \frac{W_1}{L_1}}\right)\right]. \qquad (2)$$

By rearranging $I_{\mathrm{D}}(t)/I_{\mathrm{D}}(t_0)$ one yields:

$$I_{\mathrm{D1}}(t) = I_{\mathrm{D1}}(t_0) \cdot \exp\left(\frac{\Delta\varphi_{\mathrm{G1}}(t)}{\zeta \cdot V_{\mathrm{T}}} - \zeta \cdot \frac{\Delta\varphi_{\mathrm{S1}}(t)}{\zeta \cdot V_{\mathrm{T}}}\right) \qquad (3)$$
$$= I_{\mathrm{D1}}(t_0) \cdot \exp\left(\frac{\zeta + A}{A \cdot \zeta \cdot V_{\mathrm{T}}} \cdot \Delta\varphi_{\mathrm{G1}}(t)\right). \qquad (4)$$

Using Kirchoff's current law, one can now describe the deterministic large-signal circuit behavior through the following ordinary differential equation:

$$\frac{\mathrm{d}\Delta\varphi_{\mathrm{FE}}}{\mathrm{d}t} + \frac{A \cdot I_{\mathrm{D}}(t_0)}{[1+A] \cdot C_{\mathrm{C}}} \cdot \exp\left(\frac{\zeta + A}{A \cdot \zeta \cdot V_{\mathrm{T}}} \cdot \Delta\varphi_{\mathrm{FE}}(t)\right) = \frac{A}{[1+A] \cdot C_{\mathrm{C}}} \cdot I_{\mathrm{PD}}. \qquad (5)$$

Similarly, the source follower buffer is modeled by:

$$\frac{\mathrm{d}\Delta\varphi_{\mathrm{O1}}}{\mathrm{d}t} = \frac{1}{C_{\mathrm{LSF}}} \cdot \left[I_{SF} - I_{\mathrm{D2}}(t_0) \cdot \exp\left(\frac{\zeta \cdot \Delta\varphi_{\mathrm{O1}}(t)}{\zeta \cdot V_{\mathrm{T}}} - \frac{\Delta\varphi_{\mathrm{FE}}(t)}{\zeta \cdot V_{\mathrm{T}}}\right)\right], \qquad (6)$$

with bias I_{SF} and C_{LSF} being the load seen by the buffer. Note, that this derivation assumes a PMOS buffer, but the derivation for an NMOS buffer can be made analogously.

One critical scenario used for characterization is the response to a temporal contrast change (see Fig. 1b). Using separation of variables it can be shown that the ODE in Eq. 5 has an analytical solution. The input signal:

$$I_{\mathrm{photo}}(t) = \begin{cases} I_{\mathrm{photo\text{-}0}} \text{ for } t = t_0 \\ I_{\mathrm{photo\text{-}1}} \text{ for } t > t_0 \end{cases} \qquad (7)$$

corresponds to a linear scene-level temporal contrast step:

$$C_{\mathrm{scene}} = \frac{I_{\mathrm{photo\text{-}1}} - I_{\mathrm{photo\text{-}0}}}{I_{\mathrm{photo\text{-}0}}}. \qquad (8)$$

Assuming the starting conditions: $I_{\mathrm{D1}}(t_0) = I_{\mathrm{photo}}(t_0)$ and $\Delta V_{\mathrm{FE}}(t_0) = 0$, the solution to Eq. 5 is given by:

$$\Delta v = \frac{\Delta V_{\mathrm{FE}}}{V_{\mathrm{T}} \cdot \frac{A \cdot \zeta}{\zeta + A}} = \ln\left(\frac{I_{\mathrm{photo\text{-}1}}}{I_{\mathrm{photo\text{-}0}}} \cdot \frac{1}{1 + C_{\mathrm{scene}} \cdot \exp[-[t - t_0]/\tau]}\right), \qquad (9)$$

with time-constant:

$$\tau = \frac{1+A}{A} \cdot \frac{A \cdot \zeta}{\zeta + A} \cdot \frac{V_{\mathrm{T}} \cdot C_{\mathrm{C}}}{I_{\mathrm{photo\text{-}1}}}. \qquad (10)$$

Unfortunately, separation of variables of ODE in Eq. 6 leads to transcendental terms prohibiting an analytical solution for the response of V_{O1} to a temporal contrast step in I_{photo}. Furthermore, Eq. 5 also leads to transcendental terms if driven by other input signals than contrast steps. Numerical solutions are required. At low photocurrents, the logarithmic amplifier dominates the pixel latency and the SF buffer can be approximated by its DC gain of $1/\zeta$.

Fig. 2 shows that this model yields a significant matching improvement against circuit simulations compared to [10]. Forward-Euler integration is used to solve the ODEs.

III. Small-Signal Pixel Noise Model

Noise is assumed to be a small-signal phenomenon. Simplified schematics of the logarithmic amplifier and source-follower and their small-signal equivalent representations are given in Fig. 3. Here, channel length modulation is neglected.

For NMOS $\underline{i_{\mathrm{D}}}$ is given by:

$$\underline{i_{\mathrm{D}}} = g_{\mathrm{mG}} \cdot \underline{\varphi_{\mathrm{G}}} + g_{\mathrm{mS}} \cdot \underline{\varphi_{\mathrm{S}}} \qquad (11)$$
$$g_{\mathrm{mG}} = \frac{\partial I_{\mathrm{D}}}{\partial \varphi_{\mathrm{G}}} = \frac{I_{\mathrm{D}}}{\zeta \cdot V_{\mathrm{T}}} \qquad (12)$$
$$g_{\mathrm{mS}} = \frac{\partial I_{\mathrm{D}}}{\partial \varphi_{\mathrm{S}}} = -\frac{I_{\mathrm{D}}}{V_{\mathrm{T}}} = -g_{\mathrm{mG}} \cdot \zeta. \qquad (13)$$

PMOS characteristics can be derived analogously.

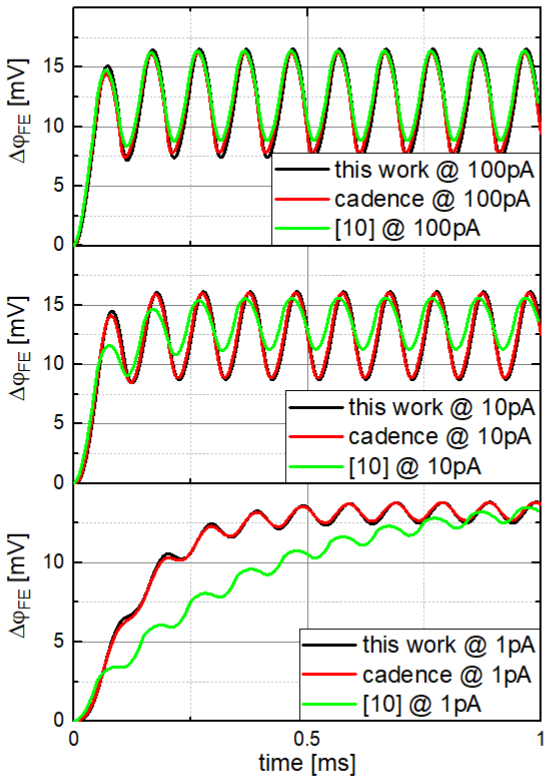

Figure 2. Evaluation of the transient model.

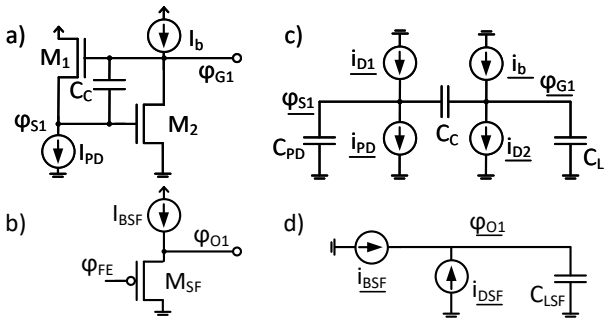

Figure 3. Simplified log-amplifier schematic a) and SF schematic b) and their respective small signal circuits in c) and d), respectively.

It is assumed that $I_\mathrm{b} \gg I_\mathrm{photo}$ such that $g_\mathrm{mG2} \gg g_\mathrm{mG1}$. Using dominant pole approximation[1] , $\underline{\varphi_\mathrm{G1}}$ results in:

$$\underline{\varphi_\mathrm{G1}} = \frac{\underline{i_\mathrm{PD}}}{g_\mathrm{mG1}} \cdot \frac{1 - j\omega/z_1}{[1 + j\omega/p_\mathrm{d1}] \cdot [1 + j\omega/p_\mathrm{nd1}]} + \frac{\underline{i_\mathrm{b}}}{g_\mathrm{mG2}} \cdot \frac{1 + j\omega/z_2}{[1 + j\omega/p_\mathrm{d2}] \cdot [1 + j\omega/p_\mathrm{nd2}]}, \quad (14)$$

with the zeros $z_1 = \frac{g_\mathrm{mG2}}{C_\mathrm{C}}$ and $z_2 = \frac{g_\mathrm{mG1} \cdot \zeta}{C_\mathrm{C}+C_\mathrm{PD}}$, dominant poles $p_\mathrm{d1} = p_\mathrm{d2} = \frac{g_\mathrm{mG1}}{C_\mathrm{C}}$ and non-dominant poles $p_\mathrm{nd1} = p_\mathrm{nd2} = \frac{g_\mathrm{mG2}}{C_\mathrm{PD} \cdot \frac{C_\mathrm{C}+C_\mathrm{PD}+C_\mathrm{L}}{C_\mathrm{C}}}$. With $p_\mathrm{d1} \ll p_\mathrm{nd1} \ll z_1$, the first transfer function can be approximated simply by neglecting p_nd1 and z_1 yielding a single-pole system. As $z_2 \ll p_\mathrm{d2} \ll p_\mathrm{nd2}$, the second transfer function first increases gain between z_2 and p_d2 and then drops like a single pole system above p_nd2. Hence, we approximate $\frac{1+j\omega/z_2}{1+j\omega/p_\mathrm{d2}} \approx \frac{p_\mathrm{d2}}{z_2}$ yielding:

$$\underline{\varphi_\mathrm{G}} \approx \frac{\underline{i_\mathrm{PD}}}{g_\mathrm{mG1}} \cdot \frac{1}{1 + j\omega \underbrace{C_\mathrm{C}/g_\mathrm{mG1}}_{=\tau_1}} + \frac{\underline{i_\mathrm{b}}}{g_\mathrm{mG2}} \cdot \frac{(C_\mathrm{C} + C_\mathrm{PD} + C_\mathrm{L})/C_\mathrm{C}}{1 + j\omega \underbrace{C_\mathrm{PD} \cdot \frac{C_\mathrm{C} + C_\mathrm{L}}{C_\mathrm{C}}/g_\mathrm{mG2}}_{=\tau_2}}. \quad (15)$$

Analogously, $\underline{\varphi_\mathrm{O1}}$ can be derived to:

$$\underline{\varphi_\mathrm{O1}} = \frac{1}{\zeta} \cdot \frac{\underline{\varphi_\mathrm{FE}}}{1 + j\omega C_\mathrm{LSF}/[\zeta \cdot g_\mathrm{mG}]} + \frac{1}{\zeta \cdot g_\mathrm{mG}} \cdot \frac{\underline{i_\mathrm{BSF}}}{1 + j\omega \underbrace{C_\mathrm{LSF}/[\zeta \cdot g_\mathrm{mG}]}_{=\tau_3}}. \quad (16)$$

Shot noise is considered to be the primary noise source for a standard pixel under regular operating conditions. In contrast, flicker noise often is negligible. However, as the power spectral density of flicker noise scales inversely with transistor size and for small devices can vary by several orders of magnitude, it can contribute to noisy pixels. Especially I_b and M_2 have to be designed with care. The goal of this work is to derive a noise model for a "standard pixel." Thus flicker noise is neglected. For weak inversion operation in the saturation domain the single-sided power spectral density is $2qI$. M_1 exhibits shot noise of the same magnitude as the photodiode given that they carry the same current under static operation and both noise sources share the same transfer characteristic. However, they are assumed uncorrelated. Similarly, M_2 and the bias I_b share the transfer function and noise magnitude and, again, are uncorrelated. Thus, the autocorrelation functions of additive noise sources at V_FE and V_O1 are:

$$R_\mathrm{FE,FE}(\Delta t) = \zeta \cdot \frac{k_\mathrm{B} \cdot \theta}{C_\mathrm{C}} \cdot e^{-\frac{|\Delta t|}{\tau_1}} + \zeta \cdot \frac{k_\mathrm{B} \cdot \theta}{\frac{C_\mathrm{PD} \cdot C_\mathrm{C} \cdot [C_\mathrm{C}+C_\mathrm{L}]}{[C_\mathrm{C}+C_\mathrm{PD}]^2}} \cdot e^{-\frac{|\Delta t|}{\tau_2}} \quad (17)$$

and

$$R_\mathrm{O1,O1}(\Delta t) = \frac{k_\mathrm{B} \cdot \theta}{C_\mathrm{LSF}} \cdot e^{-\frac{|\Delta t|}{\tau_3}}. \quad (18)$$

IV. Autoregressive Model

Fig. 4 illustrates the signal flow used by the presented EVS model. The photodiode current $I_\mathrm{PD} = I_\mathrm{photo} + I_\mathrm{dark}$ is propagated to V_FE using ODE model (Eq. 5) solved using Forward-Euler integration. Noise is added in a that matches the autocorrelation function Eq. 17. The superposition of signal and noise is then fed into the SF-buffer using Eq. 6. Now the noise contribution of the buffer is added in a way its autocorrelation function matches Eq. 18. The final result is then used to drive the difference detecting circuit which is also modeled by a simple differential equation in order to model signal dependent leak events and high-pass filter characteristic proposed in [5].

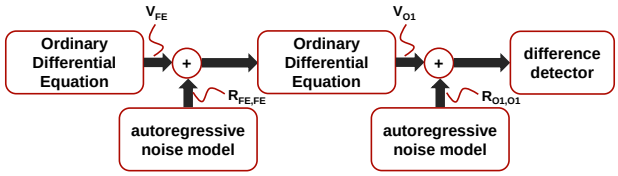

Figure 4. Pixel model signal flow diagram combining large-signal deterministic and small-signal noise behavior.

By construction, the noise models Eq. 17 and Eq. 18 describe single pole characteristics. Using Forward-Euler integration, the response X of such a system to noise e describes a first-order autoregressive model [13]:

$$X(n) = X(n-1) + [e(n) - X(n-1)] \cdot \frac{\Delta t}{\tau} \quad (19)$$

$$= \Phi_{1,1} \cdot X(n-1) + f(n), \quad (20)$$

where τ is the system time constant and Δt is the Forward-Euler time-step. $e(n) \sim \mathcal{N}(0, \sigma)$ is derived from a random number generator in order to yield a white Gaussian noise process $f(n) \sim \mathcal{N}\left(0, \sigma \cdot \frac{\Delta t}{\tau}\right)$. Choosing $E[X(0)] = 0$, it can be shown that $X(n)$ is wide-sense stationary

$$\Rightarrow E[X(n)] = 0 \quad (21)$$

$$\mathrm{var}[X] = \Phi_{1,1}^2 \cdot E[X^2(n-1)] + \sigma^2 \cdot \frac{[\Delta t]^2}{\tau^2} \quad (22)$$

$$\Rightarrow \mathrm{var}[X] = \sigma^2 \cdot \frac{\left[\frac{\Delta t}{\tau}\right]^2}{1 - \left[1 - \frac{\Delta t}{\tau}\right]^2}, \quad (23)$$

with $R_{X,X}(n) = \Phi_{1,1}^n \cdot \sigma_X^2$. Furthermore, we can show that the autocorrelation function of such an auto-regressive process $R_{X,X\text{-a.r.}}$ converges against the time-continuous $R_{X,X\text{-t.c.}}$ modeling white noise in first-order low-pass-filter systems:

[1] Dominant pole approximation expresses a transfer function by dominant p_d and non-dominant p_nd poles: $\frac{1}{1+j\omega\alpha+(j\omega)^2\cdot\beta} \approx \frac{1}{[1+j\omega/p_\mathrm{pd}]\cdot[1+j\omega/p_\mathrm{d}]}$. With $\frac{1}{[1+j\omega/p_\mathrm{pd}]\cdot[1+j\omega/p_\mathrm{d}]} \approx \frac{1}{1+j\omega/p_\mathrm{d}+(j\omega)^2/(p_\mathrm{pd}\cdot p_\mathrm{d})}$, $p_\mathrm{d} = 1/\alpha$ and $p_\mathrm{pd} = \alpha/\beta$ results.

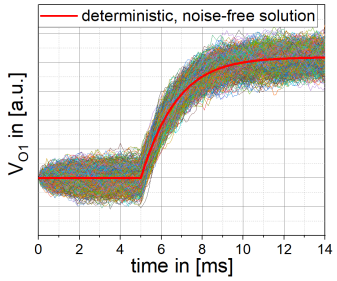

Figure 5. Sample paths of contrast step response using the deterministic ODE and the autoregressive noise model.

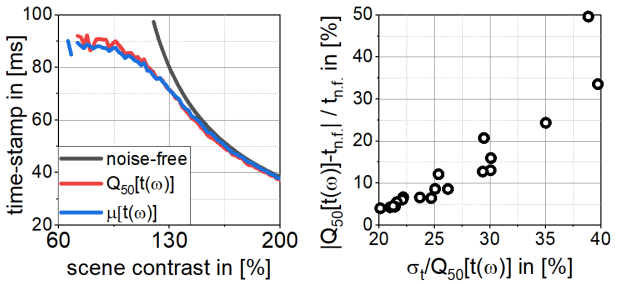

Figure 6. Comparison of noise-free time-stamp $t_{\text{n.f.}}$, median $Q_{50}[t(\omega)]$ and mean $\mu[t(\omega)]$ vs. contrast (left), and illustration of relative time-stamp variability $\sigma_t/Q_{50}[t(\omega)]$ as indicator of confidence (right).

$$R_{X,X-\text{t.c.}}(\Delta t \cdot m) = \sigma_X^2 \cdot \exp\left(-\frac{\Delta t \cdot m}{\tau}\right) \tag{24}$$

$$\approx \sigma_X^2 \cdot \left[1 - \frac{\Delta t}{\tau}\right]^m \tag{25}$$

$$= \sigma_X^2 \cdot \Phi_{1,1}^m = R_{X,X\text{-a.r.}}(m). \tag{26}$$

Rearranging Eq. 23 for σ as function of desired σ_X and τ (cf. Eq. 17, Eq. 18) and step-size Δt yields physical noise behavior of desired magnitude and bandwidth.

V. Parameter Extraction and Validation

Fig. 5 shows Monte-Carlo sample paths as well as a noise-free solution of the ODE. Fig. 6 makes the crucial observation that the noise-free time-stamp can be approximated using the mean or median of the noise-affected time-stamp, provided the scene contrast is significant enough. This in turn allows the utilization of time-stamps from contrast step measurements for model parameter estimation using an optimization approach $\vec{p}^* = \arg\min_{\vec{p}} \left\| \vec{t_i} - t_{\text{model}}(I_{\text{photo-0}}, I_{\text{photo-1}}, \vec{p}) \right\|$. In the right part of Fig. 6, it is illustrated that the relative time-stamp variability $\sigma_t/\text{median}[t(\omega)]$ can be used as indicator of confidence in this approximation. Thus it can guide the selection of data points used for model parameter extraction. Three different paths are conceivable. Firstly, the analytical solution can be utilized for parameter optimization in a way Monte-Carlo trials can be omitted (Eq. 9). Rearranging Eq. 9 for the time-stamp at which events are triggered yields

$$t_{\text{event}} = \tau \cdot \ln\left(\frac{C_{\text{scene}} \cdot [1 + C_\infty]}{C_{\text{scene}} - C_\infty}\right), \tag{27}$$

with $C_\infty = \exp\left[\frac{V_{\text{threshold}}}{V_T \cdot (1+\zeta) \cdot G}\right] - 1$ and G being the difference detector gain and $V_{\text{threshold}}$ the trigger level of the comparators. t_{event} shows a dependency of τ and the characteristic threshold C_∞ that can be interpreted as contrast threshold if the pixel would exhibit no noise. Combining a set of contrast steps at varying starting radiance yields independent measurements suitable to extract both parameters jointly. Secondly, a numerical solution can take into account the transient impact of M_{SF}. Lastly, to utilize low-contrast steps, the impact of noise needs to be considered using the autoregressive model. Note that alternatively to fitting time-stamps, one can also fit event firing probabilities. However, here, clearly noise can never be neglected. We measured devices of [5], extracted parameters, and compared measurements vs. simulations in Fig. 7 yielding good resemblance.

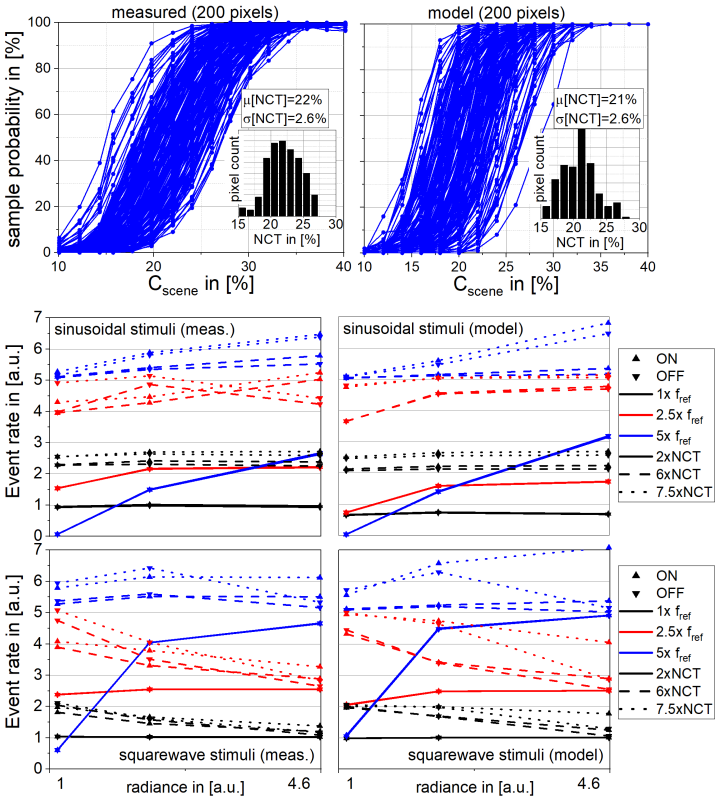

Figure 7. Comparison of measured pixel-level S-curves (top-left) vs. model (top-right), measured response to sinusoidal stimulus (middle-left) vs. model (middle-right) and measured response to squarewave stimulus (bottom-left) vs. model (bottom-right) across a 4.6x radiance, a 7.5x contrast and a 5x frequency range.

VI. Conclusion

We present a physical model for EVS pixels improving accuracy for latency and noise phenomena. We outline three paths for parameter extraction and demonstrated good model resemblance to circuit simulations as well as measurements.

References

[1] P. Lichtensteiner et al., PhD thesis, ETH, 2006.
[2] G. Gallego et al., IEEE TPAMI, Vol. 44, No. 1, pp. 154-180, Jan. 2022.
[3] T. Finateu et al., IEEE ISSCC, pp. 112-114, Feb. 2020.
[4] Y. Suh et al., IEEE ISCAS, pp. 1-5, Oct. 2020.
[5] M. Guo et al., IEEE ISSCC, pp. 90-92, Feb. 2023.
[6] K. Kodama et al., IEEE ISSCC, pp. 92-94, Feb. 2023.
[7] H. Rebecq et al., CoRL, Oct. 2018.
[8] D. Gehrig et al., IEEE CVPR, pp. 3586-3595, June 2020.
[9] Y. Hu et al., IEEE CVPR, pp. 1312-1321, June 2021.
[10] X. Mou et al., Proc. IS&T EI, ISS-242, Jan. 2022.
[11] C. Posch et al., IEEE ISCAS, pp. 1572-1575, May 2011.
[12] B. McReynolds et al., Opt. Eng., 61(7) 074103, July 2022.
[13] K.S. Shanmugan and A.M. Breiphol, *Random Signals*, Wiley, July 1988.